

Chloride impurity induced corrosion of nickel anode and its protection in molten $\text{Li}_2\text{CO}_3\text{-Na}_2\text{CO}_3\text{-K}_2\text{CO}_3$

Peilin Wang, Kaifa Du, Mengyi Tang, Huayi Yin, Dihua Wang*

School of Resource and Environmental Science, Hubei International Scientific and Technological Cooperation Base of Sustainable Resources and Energy, Wuhan University, Wuhan 430072, China



ARTICLE INFO

Keywords:

- A. Nickel
- A. Molten salts
- C. Anodic films
- C. High temperature corrosion
- C. Pitting corrosion

ABSTRACT

It is well-known that Cl^- can cause localized corrosion of metal in aqueous solutions, but its effect on material corrosion under anodic polarization in molten salts is less known. Herein, the effect of Cl^- on the stability of nickel anode in molten $\text{Li}_2\text{CO}_3\text{-Na}_2\text{CO}_3\text{-K}_2\text{CO}_3$ was investigated. There existed a critical corrosion concentration of Cl^- (0.2 mol% at 650 °C), above which serious corrosion of nickel anode took place. Cl^- reduced the compactness and adherence of oxide scales. It was found that the addition of CaCO_3 can effectively protect nickel anode from Cl^- induced corrosion by increasing the electrolyte basicity.

1. Introduction

Molten carbonate electrolysis (MCE) powered by renewable electricity is showing promising potential in achieving carbon-neutral [1–3], which has been applied to low-carbon metallurgy and CO_2 fixation [4, 5]. Fe, Ni, Co and their alloys have been prepared through the electrochemical reduction of solid oxides in molten carbonate [5–8]. Moreover, electrochemical reduction of CO_2 in molten carbonate offers an attractive approach to producing value-added carbonaceous materials and chemicals while mitigating greenhouse gas emissions [1,4,9–11]. During the electrolysis, metal oxides and/or CO_2 -capture-generated CO_3^{2-} are reduced on the cathode. Subsequently, the released oxide ions are conducted through the electrolyte and migrate to the anode, where they oxidatively recombine into O_2 [1,4]. Thus, a stable oxygen-evolution inert anode is key to enabling the success of the MCE processes. However, the service stability of inert anodes is challenged by the highly corrosive working environment, i.e., strong anodic polarization in molten salts at elevated temperatures [4,12]. Up till now, metallic materials have been considered as one of the most promising candidate materials of inert anode due to their excellent mechanical robustness and high electronic conductivity [12–15]. Apart from the noble metal anodes such as platinum coating electrode [16], the more cost-affordable nickel and nickel-based alloys have been confirmed to work stably as oxygen-evolution inert anodes, which ensures the operation of the MCE process [17–21].

Despite the encouraging advances on inert anodes for the MCE

process, the effect of impurities in molten carbonate electrolyzers on inert anodes has received little attention for a long time. In consideration of the cost and technical difficulty of salt purification [22,23], industrial-grade carbonate salts are usually used without further purification for large-scale molten salt electrolysis. Therefore, several aggressive impurities such as chloride and sulfate could be inevitably introduced in molten carbonate electrolyzers. These impurities come from the raw materials used for preparing carbonate salts [24,25]. In addition, if unpurified CO_2 such as coal-fired flue gas is used as feeding gas into molten carbonate electrolyzers, traces of SO_2 and HCl in flue gas will be simultaneously captured by molten carbonate [11,26]. This also could lead to the formation and accumulation of chloride and sulfate impurities in the electrolytes.

Our recent work revealed that SO_4^{2-} impurity produced a negative effect on the stability and lifetime of nickel anodes in molten $\text{Li}_2\text{CO}_3\text{-Na}_2\text{CO}_3\text{-K}_2\text{CO}_3$ [27]. In practice, chloride is also among the most deleterious impurities from the viewpoint of corrosion and it is extremely hard to remove completely [28,29]. It is well known that the passive layer on metallic materials is susceptible to severe localized attack in chloride-containing media [28,30,31]. Moreover, chloride salts could cause hot corrosion of nickel-based alloys at elevated temperatures [13, 29,32,33]. Therefore, it is urgent to reveal the relationships between chloride content and lifetime of nickel anodes, which is crucial for the development of long-lasting inert anodes.

In this work, the effect of chloride on the stability of nickel anodes in molten $\text{Li}_2\text{CO}_3\text{-Na}_2\text{CO}_3\text{-K}_2\text{CO}_3$ was systematically studied, and the Cl^-

* Corresponding author.

E-mail address: wangdh@whu.edu.cn (D. Wang).

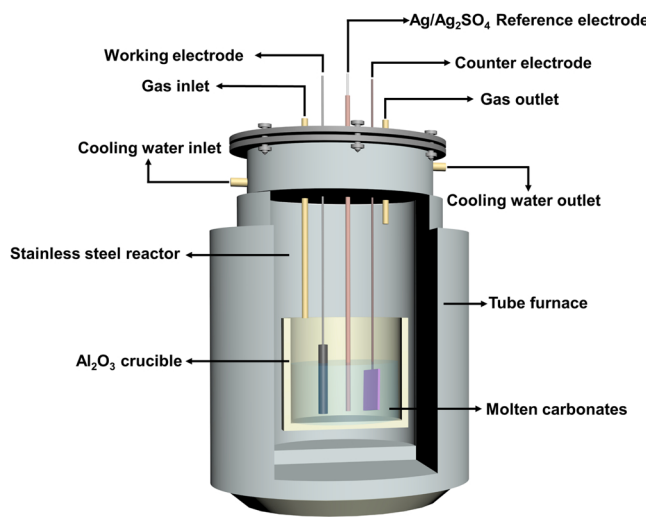


Fig. 1. The schematic diagram of the experimental set-up for corrosion tests.

Table 1

Thermodynamic data of possible anodic reactions for the calculation of potential-basicity diagram.

No.	Reactions	$\Delta G^{\circ}/\text{kJ mol}^{-1}$	$E^{\circ}/\text{V vs. Li}^{+}/\text{Li}$
1	$\text{O}_2(\text{g}) + 4\text{Li}^{+} + 4\text{e}^{-} = 2\text{Li}_2\text{O}$	224.081	2.467
2	$\text{NiCl}_2 + 2\text{Li}^{+} + 2\text{e}^{-} = \text{Ni} + 2\text{LiCl}$	87.166	2.596
3	$\text{NiO} + 2\text{Li}^{+} + 2\text{e}^{-} = \text{Ni} + \text{Li}_2\text{O}$	267.310	1.662
4	$\text{LiNiO}_2 + \text{Li}^{+} + \text{e}^{-} = \text{NiO} + \text{Li}_2\text{O}$	60.110	2.425
5	$\text{Li}^{+} + \text{e}^{-} = \text{Li}$	293.887	0
6	$\text{NiCl}_2 + \text{Li}_2\text{O} = \text{NiO} + 2\text{LiCl}$	-180.224	/
7	$\text{Li}_2\text{CO}_3 = \text{Li}_2\text{O} + \text{CO}_2(\text{g})$	82.389	/
8	$\text{CaCO}_3 = \text{CaO} + \text{CO}_2(\text{g})$	34.296	/

induced corrosion mechanism was revealed. Based on the proposed corrosion mechanism, a certain amount of CaCO_3 was added into Cl^- -containing molten carbonate to protect the nickel anodes from corrosion.

2. Material and methods

2.1. Preparation of electrolytes and electrodes

All chemicals were of analytical purity and used without further purification. Anhydrous Li_2CO_3 , Na_2CO_3 , K_2CO_3 , CaCO_3 and KCl were all purchased from Sinopharm Chemical Regent Co., Ltd., China. The nickel plates and nickel rods (5 mm in diameter) used in this study were

all purchased from Shengshida metal materials Co., Ltd. Prior to the corrosion tests, the nickel plates were ground with SiC papers from 400, 1000, 3000–5000 grits successively, then ultrasonically cleaned with deionized water and acetone, and finally dried in a vacuum oven for further use.

An alumina crucible containing 500 g $\text{Li}_2\text{CO}_3\text{-Na}_2\text{CO}_3\text{-K}_2\text{CO}_3$ salts (43.5: 31.5: 25.0 in molar ratio) and a certain amount of KCl was put into a sealed vertical tubular furnace. The well-mixed salts were dried at 300 °C for more than 12 h and then heated to the target temperature under an argon atmosphere. To further remove the impurities and residual water in the molten salts, pre-electrolysis was performed at constant cell voltage of 1.5 V for 2 h by using a platinum plate and a nickel plate. In order to evaluate the protection performance of CaCO_3 on nickel anodes, a certain amount of CaCO_3 was weighted accurately and then added into the melt. The corresponding CaCO_3 addition in various experiments were 0 wt%, 5 wt% and 10 wt%, respectively.

2.2. Electrochemical measurements and corrosion tests

The schematic diagram of the experimental set-up used in this study is given in Fig. 1. Linear sweep voltammetry (LSV) was conducted with a three-electrode system controlled by an electrochemical workstation (CS310H, Wuhan Correst Instruments Co., Ltd.) in molten carbonate containing various contents of Cl^- under an argon atmosphere. Nickel wires (1 mm in diameter, 12 mm deep in electrolyte) and a nickel sheet (contact area of 80 cm^2) were employed as working electrodes (WE) and counter electrode (CE), respectively. A home-made $\text{Ag/Ag}_2\text{SO}_4$ electrode was used as the reference electrode (RE), which was prepared by inserting a silver wire into an alumina tube filled with 1 g $\text{Li}_2\text{CO}_3\text{-Na}_2\text{CO}_3\text{-K}_2\text{CO}_3$ mixed salts (molar ratio of 43.5: 31.5: 25.0) containing 0.1 mol/kg Ag_2SO_4 .

All the galvanostatic electrolysis was carried out by a two-electrode system consisting of a nickel sheet (20 mm × 30 mm × 0.1 mm) cathode and a nickel plate (10 mm × 10 mm × 1 mm) anode under various gas atmospheres. In this study, the argon gas was with ultra-high-purity (99.999%) and directly used without the purification and moisture removal treatments. The flow rates of these three types of gases were all set as 150 mL/min. The electrolysis was performed by a computer-controlled DC power source (Shenzhen Neware Electronic Ltd., China) in molten carbonate. During the electrolysis, the anode potential evolution was real-time monitored using the above-mentioned three-electrode configurations on an electrochemical workstation.

After the electrolysis, the samples were ultrasonically washed in deionized water to completely remove the residual salts and corrosion products. Then the remaining electrodes were measured using an analytical balance after drying. Weight change Δm (g/cm^2) was calculated by measuring the electrode mass before and after the electrolysis according to Eq. (1):

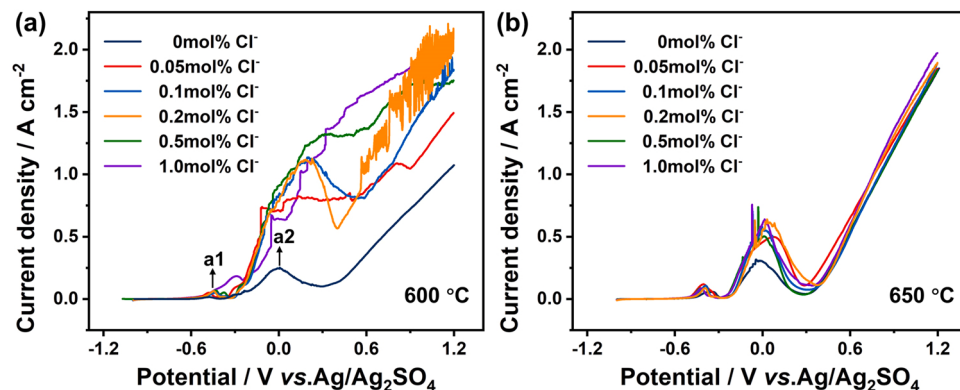


Fig. 2. Anodic polarization curves of nickel electrodes in molten $\text{Li}_2\text{CO}_3\text{-Na}_2\text{CO}_3\text{-K}_2\text{CO}_3$ containing different contents of Cl^- under an argon atmosphere at 600 °C (a) and 650 °C (b), scan rate: 5 mV/s.

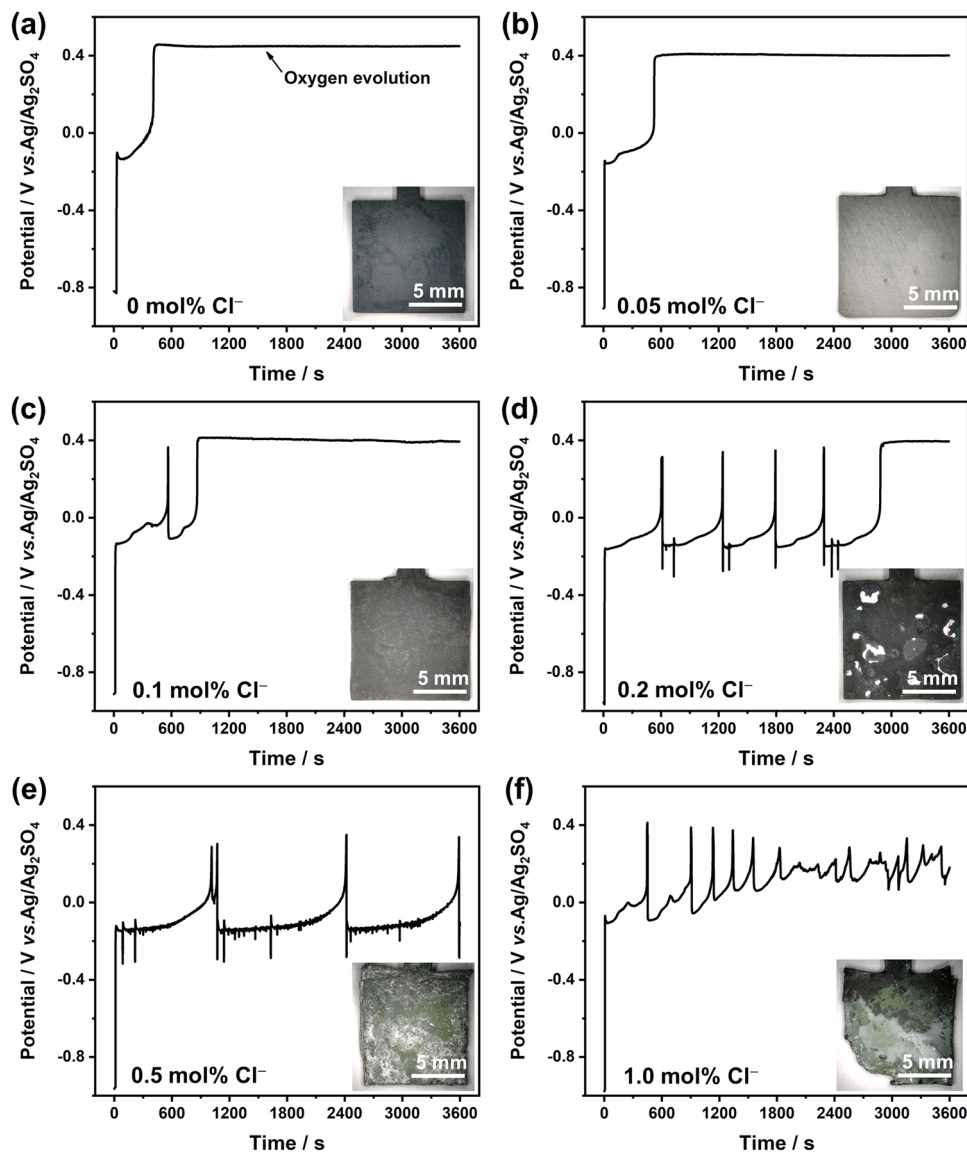


Fig. 3. Anode potential evolution over time during the galvanostatic electrolysis for 3600 s at $I_{\text{anode}} = 150 \text{ mA}/\text{cm}^2$ in molten $\text{Li}_2\text{CO}_3\text{-Na}_2\text{CO}_3\text{-K}_2\text{CO}_3$ containing different contents of Cl^- at 650°C under an argon atmosphere, the inset graphs are the optical images of nickel electrodes after the electrolysis.

$$\Delta m = \frac{W_2 - W_1}{S} \quad (1)$$

where Δm is the weight change of nickel anode. W_1 and W_2 are weights of the anode before and after the electrolysis, respectively, and S is the anode surface area immersed in the electrolyte. The symbols of plus (+) and minus (-) were used to denote the weight gain and weight loss, respectively.

2.3. Thermodynamic analysis for potential-basicity diagram of nickel

To construct the potential-basicity diagram of nickel, the possible anodic reactions in molten carbonate are summarized in Table 1. The thermodynamic data of LiNiO_2 was found in the literature [34], and the thermodynamic data of other species involved in the reactions were obtained by HSC Chemistry 5. The relationships between the Nernst potential and O^{2-} activity were calculated from the Gibbs free energies of considered reactions at 650°C by Nernst equations. To simplify the calculation, the activities of species except for Li_2O are all assumed to be

at the unit activity ($a = 1$) or stand pressure ($p = p_{\text{atm}}$). For example, the Nernst potential of oxygen evolution reaction can be given by Eq. (2):

$$E = E^\theta - \frac{2.3RT}{nF} \times \lg \frac{(a_{\text{O}_2})^2}{P_{\text{O}_2}} = E^\theta - \frac{2 \times 2.3RT}{nF} \times \lg a(\text{Li}_2\text{O}) \quad (2)$$

where E and E^θ represent the Nernst potential and standard potential, respectively. P_{O_2} and a_{O_2} denote O_2 partial pressure and the activity of O^{2-} , respectively. n represents the electron transfer number, F is the Faraday constant (96,485 C/mol), and R is the gas constant (8.314 J K $^{-1}$ mol $^{-1}$).

2.4. Characterization of corrosion products

After the electrolysis, the nickel electrodes obtained in different electrolytes were washed by deionized water to remove solidified melt, rinsed by anhydrous ethanol, and dried in a vacuum oven at 80°C for 12 h. Some samples were directly kept in a vacuum oven without washing in order to prevent the spallation of corrosion scales.

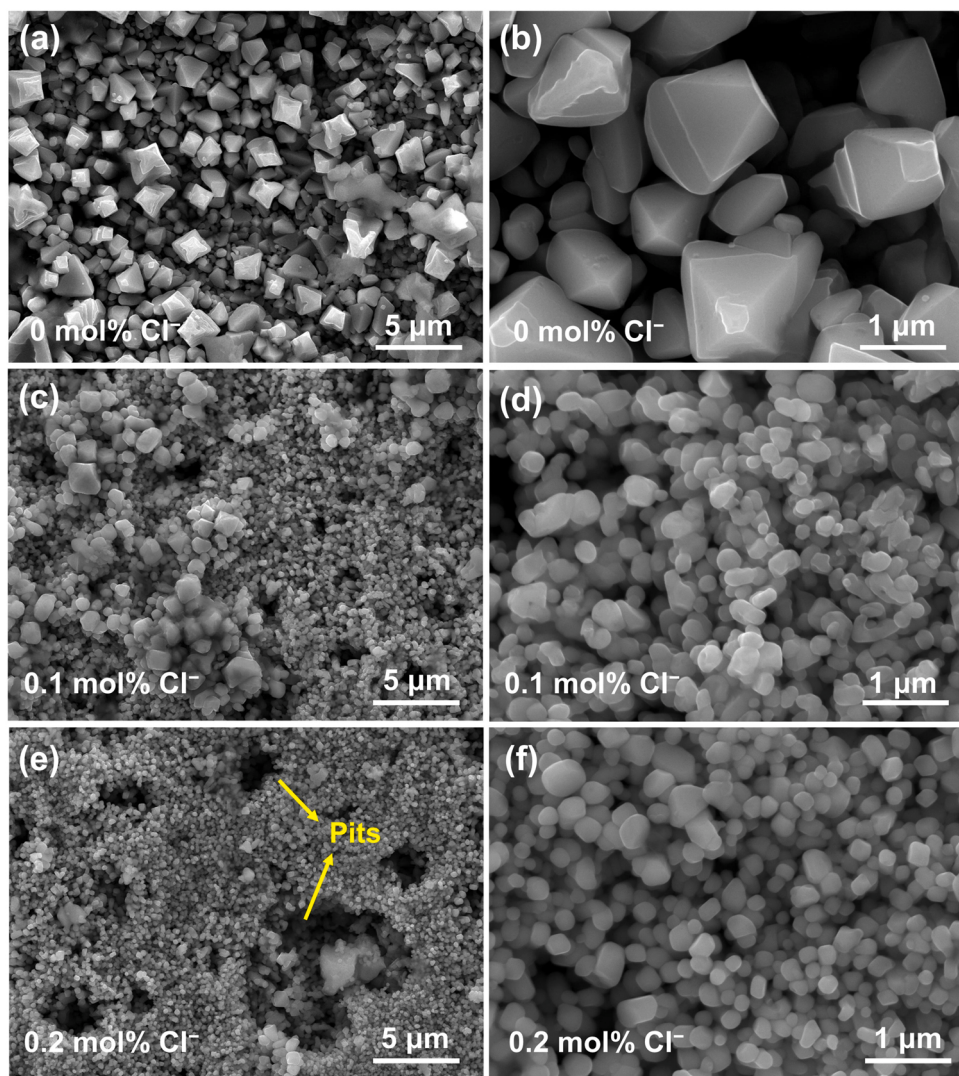


Fig. 4. SEM images of nickel electrodes after the galvanostatic electrolysis in molten $\text{Li}_2\text{CO}_3\text{-Na}_2\text{CO}_3\text{-K}_2\text{CO}_3$ without Cl^- (a-b) or containing 0.1 mol% Cl^- (c-d) and 0.2 mol% Cl^- (e-f) at 650 °C under an argon atmosphere.

Afterwards, the obtained samples were characterized by 3-D optical microscope (Keyence VHX-5000), X-ray diffraction spectroscopy (XRD, Shimadzu X-ray 6000 with Cu K α 1 radiation at 40 kV and 250 mA, $\lambda = 0.154$ nm) and scanning electron microscopy (SEM, TESCAN MIRA 3 LMH). Several selected specimens were embedded in epoxy resin, ground with SiC papers and then polished with fine diamond paste in cross-section. The morphology and chemical compositions of corrosion layer were characterized by SEM with back-scattered electron (BSE) mode and energy dispersive spectrometer (EDS, Oxford X-max 20).

3. Results and discussion

3.1. Electrochemical measurements

Fig. 2 shows the anodic polarization curves of nickel in molten $\text{Li}_2\text{CO}_3\text{-Na}_2\text{CO}_3\text{-K}_2\text{CO}_3$ containing different contents of Cl^- . As shown in **Fig. 2a**, the anodic behaviors of nickel at 600 °C were strongly dependent on the Cl^- concentration. In Cl^- -free electrolyte, Ni exhibited typical activation-passivation transition behaviors. There were two anodic current peaks (a1 and a2) prior to oxygen evolution, which corresponded to the oxidation of nickel to Ni(II) and Ni(III), respectively [21].

However, the current density in passive region significantly increased and the passive region became narrow with increasing Cl^- concentration in the electrolyte. This suggests that the passivity of nickel anodes broke down in the presence of Cl^- , and thus the corrosion rate of nickel anodes was significantly increased.

At 650 °C, Ni exhibited the passivation and oxygen evolution behaviors in all test electrolytes (**Fig. 2b**), indicating the lower susceptibility of nickel anodes to Cl^- at higher temperatures. This is because stable NiO rather than unstable LiNiO_2 is prone to form on the surface of nickel plate at above 600 °C. However, there were also several current spikes observed in the polarization curves, which corresponds to the metastable pitting events involving the nucleation and re-passivation processes of corrosion pits. Besides, the oxidation current of peak a2 increased and the current fluctuations in the passive region became more remarkable with increasing Cl^- concentration. This demonstrated that nickel anodes gradually became unstable with increasing Cl^- concentration.

It is generally considered that the transition from metastable pit to stable pit formation might occur after an initial incubation protective period [35,36]. Therefore, galvanostatic electrolysis for long time was conducted to further evaluate the pitting corrosion tendencies of nickel

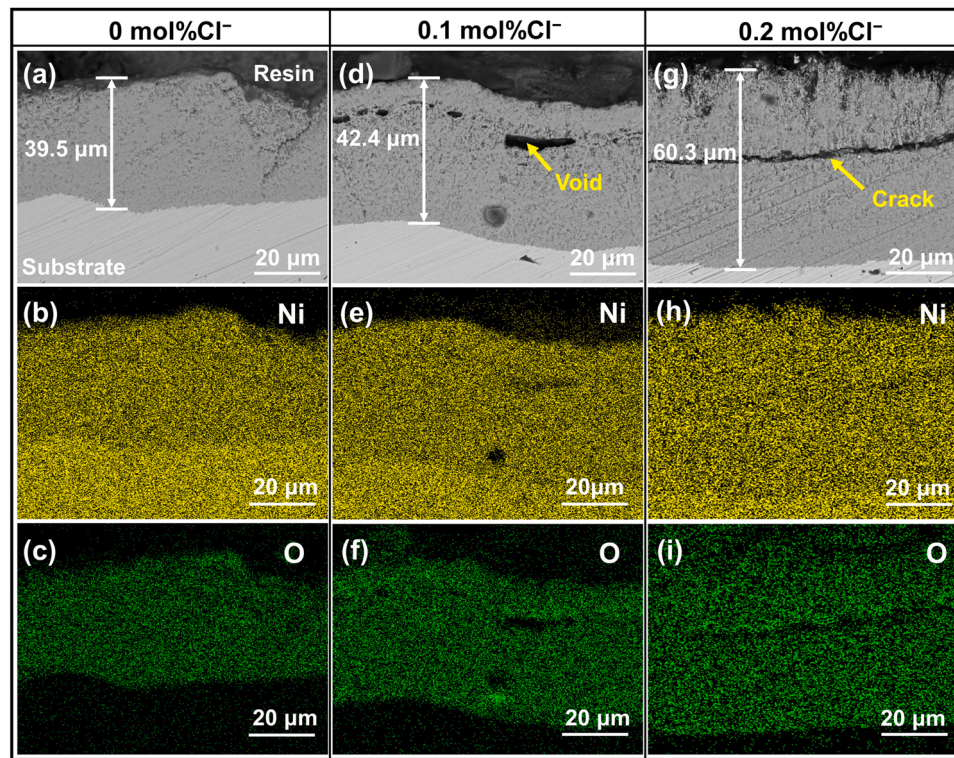


Fig. 5. Cross-sectional SEM images in the backscattered electrons (BSE) mode and corresponding EDS mapping images of the nickel electrodes after the galvanostatic electrolysis in molten $\text{Li}_2\text{CO}_3\text{-Na}_2\text{CO}_3\text{-K}_2\text{CO}_3$ without Cl^- (a–c) or containing 0.1 mol% Cl^- (d–f) and 0.2 mol% Cl^- (g–i) at 650 °C under an argon atmosphere.

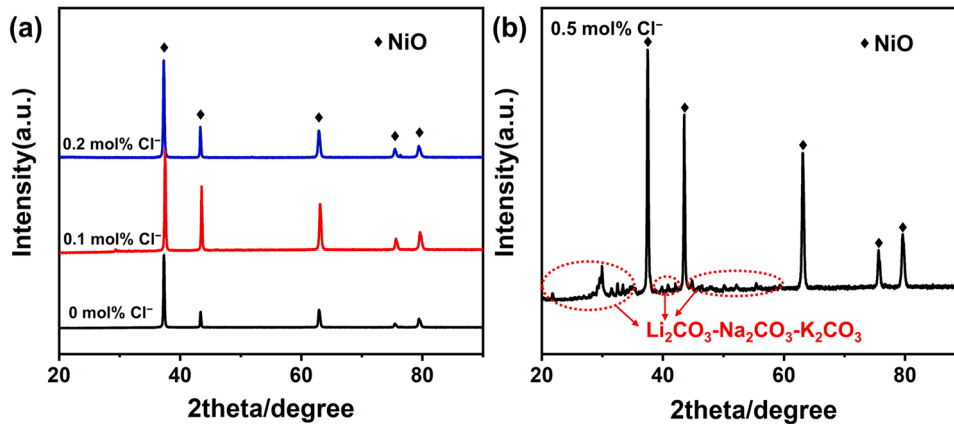


Fig. 6. XRD patterns of nickel electrodes after the galvanostatic electrolysis in molten $\text{Li}_2\text{CO}_3\text{-Na}_2\text{CO}_3\text{-K}_2\text{CO}_3$ without Cl^- or containing 0.1 mol%, 0.2 mol% (a) and 0.5 mol% (b) Cl^- at 650 °C under an argon atmosphere.

anodes at 650 °C. The anode potential-time plots during the galvanostatic electrolysis in molten $\text{Li}_2\text{CO}_3\text{-Na}_2\text{CO}_3\text{-K}_2\text{CO}_3$ containing different contents of Cl^- are shown in Fig. 3. In all experiments, anode potential moved positively from open circuit potential to ~0.2 V in the initial stage of electrolysis, which was related to the electrochemical oxidation of nickel substrate. Afterwards, the change of anodic potential was related to the Cl^- concentration in molten carbonate. When the Cl^- concentration was below 0.2 mol%, the anode potential increased to ~0.4 V by shifting the anodic reaction to oxygen evolution, and it maintained steady during the subsequent electrolysis processes. This suggests that a passive scale formed and protected the nickel substrate from further dissolution. Besides, it was noted that the time required to reach the oxygen evolution potential increased with increasing Cl^-

concentration (Fig. 3a–c), demonstrating that Cl^- retarded the formation of protective oxide scale. In the melt containing 0.2 mol% Cl^- , anode potential did not reach a steady state until 3000 s of electrolysis (Fig. 3d). The sudden drops of anode potential in the passive region were due to the nucleation and re-passivation processes of corrosion pits. When the Cl^- concentration was above 0.2 mol%, anode potentials could not reach a steady state during the whole electrolysis (Fig. 3e and f). The anodic reaction was mainly the dissolution/oxidation of nickel substrate rather than oxygen evolution. Moreover, the periodical forming and stripping of the oxide scale led to the potential oscillations, indicating that the addition of Cl^- could seriously damage the passive scales.

Overall, the corrosion of nickel anodes was accelerated with increasing Cl^- concentration and there was a critical concentration of

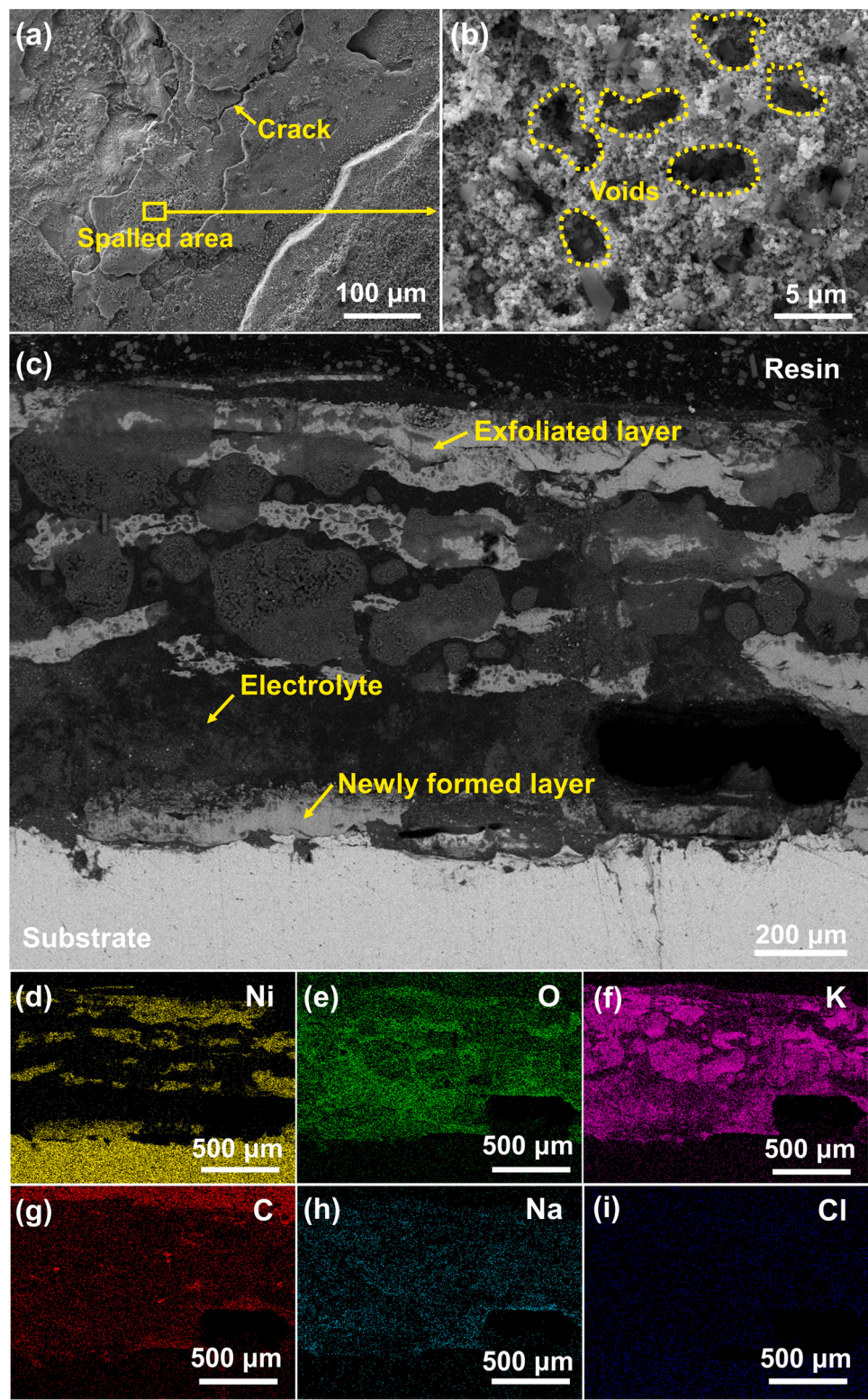


Fig. 7. SEM images (a-b), Cross-sectional SEM images in the backscattered electrons (BSE) mode and corresponding EDS mapping images (c-i) of nickel electrodes after the galvanostatic electrolysis in molten $\text{Li}_2\text{CO}_3\text{-Na}_2\text{CO}_3\text{-K}_2\text{CO}_3$ containing 0.5 mol% Cl^- at 650 °C under an argon atmosphere.

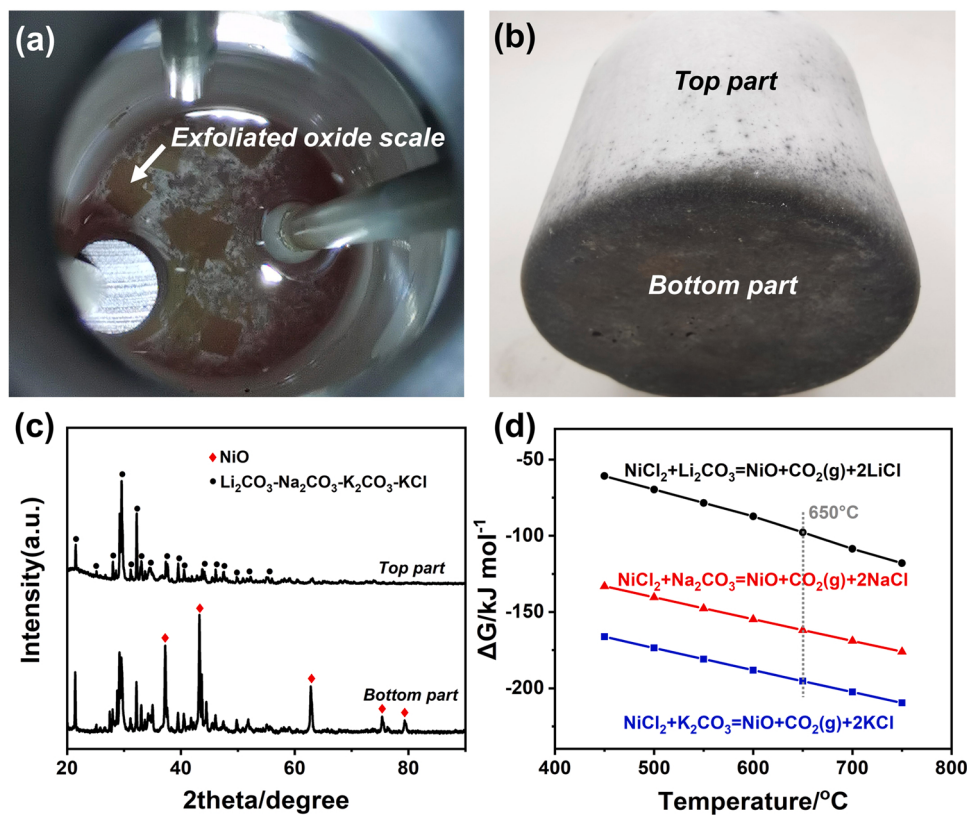


Fig. 8. Photos of the salt mixture of $\text{Li}_2\text{CO}_3\text{-Na}_2\text{CO}_3\text{-K}_2\text{CO}_3$ containing 0.5 mol% Cl^- after corrosion tests in molten state at 650 °C (a) and solid state at 25 °C (b), respectively, XRD patterns of two parts from the frozen electrolyte (c), profiles of Gibbs free energies of reactions between NiCl_2 and various carbonate salts as a function of temperature (d).

Cl^- , i.e., 0.2 mol% at 650 °C. Nickel anodes worked stably due to the formation of protective oxide scales below the critical Cl^- concentration, whereas they were corroded seriously above the critical Cl^- concentration.

3.2. Characterization of corrosion products

In order to further investigate the corrosion mechanism of nickel anodes in Cl^- -containing electrolyte, the corrosion products on the nickel plates after polarization were characterized. When the Cl^- concentration was below 0.2 mol%, nickel plates were all covered by dark and compact oxide scales (Fig. 3a–c). By contrast, the oxide scales formed in the electrolyte containing 0.2 mol% Cl^- were so poorly adherent that they were partially delaminated from the nickel substrate and the electrolyte penetrated into the oxide scales (Fig. 3d). As shown in Fig. 4, the SEM images demonstrate that the micromorphology of the oxide scales was significantly changed by the addition of Cl^- . The oxide scales formed in Cl^- -free electrolyte exhibited regular and homogenous octahedral morphology (Fig. 4a and b). In Cl^- -containing electrolyte, some corrosion pits on the surface of oxide scales were observed (Fig. 4c and e), and the sizes of corrosion pits became larger with increasing Cl^- concentration. Besides, the oxide particles distributed on the scale surface were quasi-spherical with a size of ~200 nm (Fig. 4d and f).

Furthermore, the cross-sectional SEM morphology and corresponding EDS-mapping were characterized and illustrated in Fig. 5. The oxide scale formed in Cl^- -free electrolyte was continuous and compact, which was attached closely to the substrate (Fig. 5a–c). EDS maps suggest that Ni and O were homogeneously distributed in the oxide scale with a thickness of ~39.5 μm . Combined with the XRD patterns (Fig. 6a), the oxide scale could be identified as NiO , which has been confirmed to be a

protective layer against molten carbonate corrosion [19,20]. Note that the thickness of oxide scales increased with increasing Cl^- concentration, which agrees with the increase of oxidation time induced by chloride (Fig. 3). However, the oxide scales formed in Cl^- -containing electrolyte showed a significantly higher porosity than that in Cl^- -free electrolyte (Fig. 5d–g). The formed cracks and voids in oxide scales might act as channels for the transformation of oxygen and electrolyte, which significantly promoted the oxidation rate of nickel anodes.

When the Cl^- concentration was above 0.2 mol%, nickel anodes underwent destructive corrosion. The loose and dark green corrosion scales formed and were poorly adhered to the substrate, resulting in a large amount of electrolyte penetration into the inner layer (Fig. 3e and f). The sample obtained in the electrolyte containing 0.5 mol% Cl^- was selected for further characterization. As shown in Fig. 7a, severe scale spallation was observed and the corrosion scale exhibited the rough and wrinkled structure due to the growth stress concentration during the fast oxidation process. The high-magnification SEM image in the spalled area reveals that voids accumulated and coalesced to form pores between two oxide layers (Fig. 7b). Besides, the cross-sectional SEM image shows that new oxide scales formed after the electrolyte penetrated into nickel substrate (Fig. 7c). Therefore, the sandwich-like structure consisting of the exfoliated oxide scale/the frozen electrolyte/the newly formed oxide scale was observed. Combining the elemental distributions (Fig. 7d–i) with the XRD result (Fig. 6b), the corrosion product was identified as NiO . Although NiO has a low solubility in molten $\text{Li}_2\text{CO}_3\text{-Na}_2\text{CO}_3\text{-K}_2\text{CO}_3$ [37], these oxide scales with poor adherence and compactness were considered to be unprotective to the nickel substrate.

In addition, it is worth noting that NiCl_2 was not detected within the corrosion layers and electrolyte (Fig. 7d). As shown in Fig. 8a, the salt mixture of $\text{Li}_2\text{CO}_3\text{-Na}_2\text{CO}_3\text{-K}_2\text{CO}_3$ containing 0.5 mol% Cl^- was clear

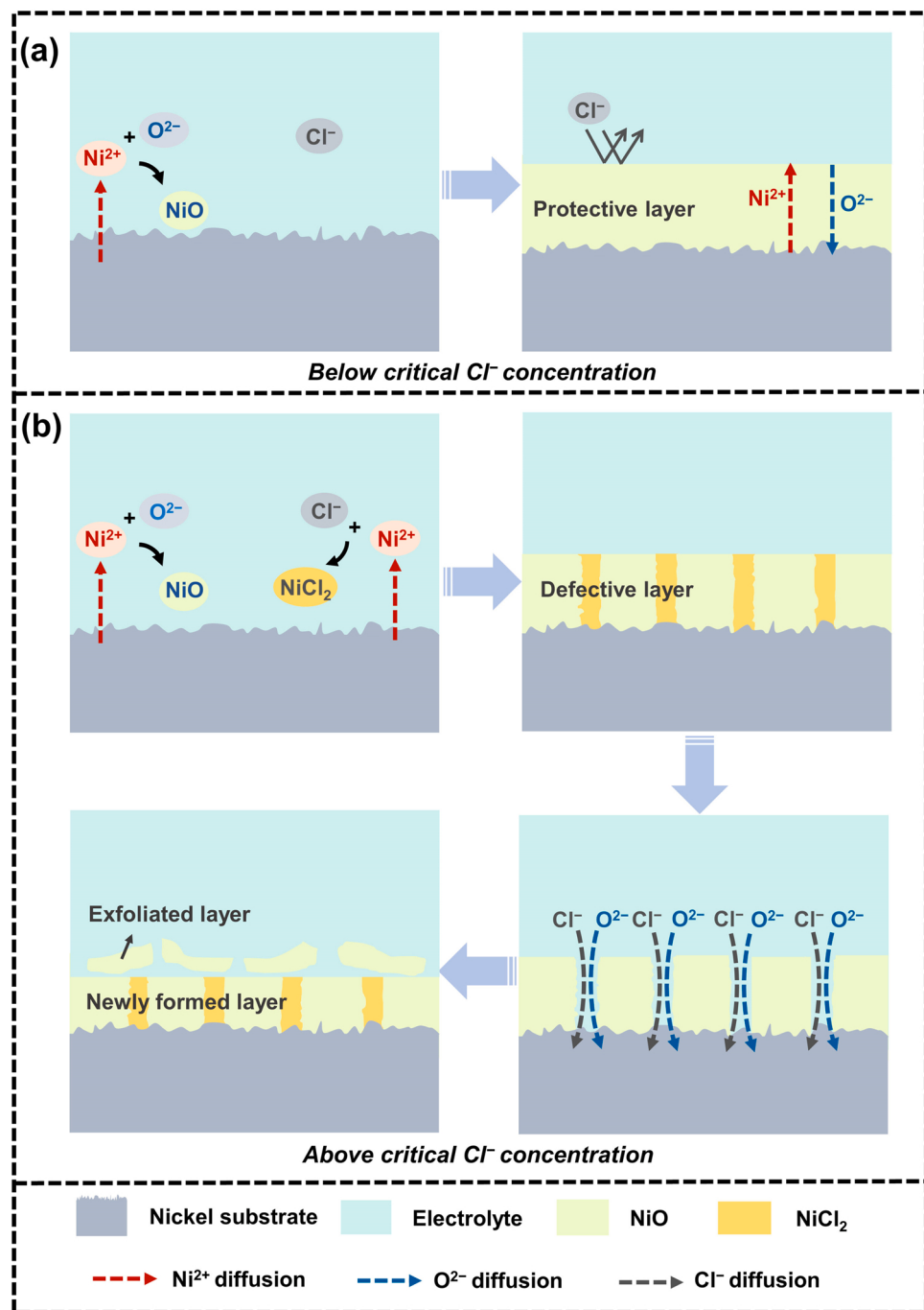


Fig. 9. Schematic of the corrosion processes of nickel anodes after anodic polarization in the electrolytes containing various contents of Cl^- .

and without color change after the electrolysis. Moreover, the corrosion scales were completely delaminated from the substrate and fallen in the electrolyte. The corrosion scales were insoluble in molten carbonate, and thus they were accumulated at the bottom of crucible. After the reactor was cooled down to room temperature, the top part of the frozen electrolyte was white, while the very bottom part became black (Fig. 8b). XRD pattern identifies that the black insoluble corrosion product at the bottom of the crucible was NiO (Fig. 8c). NiCl_2 was not detected within both the top and the very bottom parts of the frozen electrolyte, which is mainly attributed to the thermodynamic instability of NiCl_2 . Fig. 8d shows the profiles of Gibbs free energies of reactions between NiCl_2 and carbonate salts as a function of temperature, which

was calculated using HSC chemistry 5 thermodynamics software. At 650 °C, the Gibbs free energy of these three reactions are all negative, suggesting that the formed NiCl_2 could be spontaneously transformed to NiO.

Overall, the solubility of NiO in the electrolyte kept almost unchanged after the addition of Cl^- . However, the compactness and adherence of NiO scales were significantly reduced above the critical Cl^- concentration, and thus corrosion of nickel anodes was greatly accelerated.

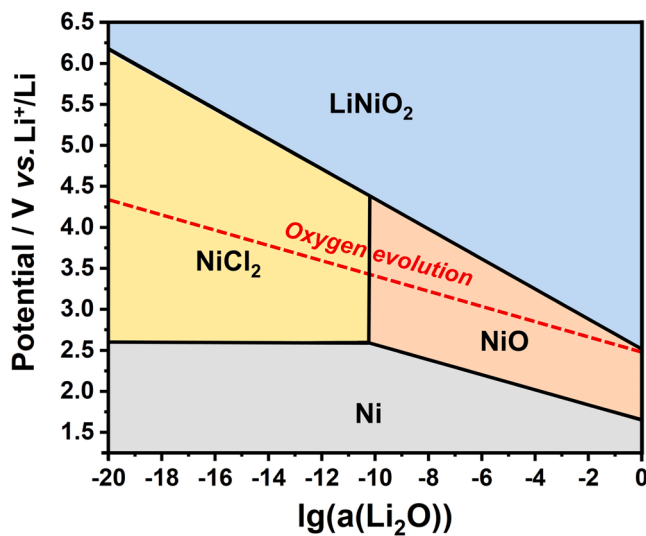


Fig. 10. Potential-basicity diagram calculated for Ni in the molten $\text{Li}_2\text{CO}_3\text{-Na}_2\text{CO}_3\text{-K}_2\text{CO}_3$ at 650°C .

Table 2

The corresponding melt composition and gas atmosphere in each case of galvanostatic electrolysis.

Case	Cl^- concentration	CaCO_3 concentration	Gas atmosphere
1	1 mol%	0 wt%	Ar
2	1 mol%	5 wt%	Ar
3	1 mol%	0 wt%	14 vol% CO_2 -Ar
4	1 mol%	5 wt%	14 vol% CO_2 -Ar
5	1 mol%	10 wt%	14 vol% CO_2 -Ar
6	2 mol%	10 wt%	14 vol% CO_2 -Ar

3.3. Chloride induced corrosion mechanism of nickel anodes

Based on electrochemical measurements and characterization of corrosion products, the chloride induced corrosion mechanism of nickel anode was proposed and illustrated in Fig. 9. The corrosion behaviors of nickel anodes were strongly dependent on the Cl^- concentration in molten carbonate. When the Cl^- concentration was below the critical concentration, the nickel anodes were covered by a dense and continuous NiO scale, which can act as the protective layer against oxygen and aggressive chloride. However, when the Cl^- concentration was above the critical concentration, NiCl_2 will form at the metal/scale interface along with NiO in the initial stage of anodic oxidation through reactions (3) and (4):



Then, the soluble NiCl_2 transfer outward and spontaneously react with the carbonate salts to regenerate NiO at the scale/electrolyte interface according to the reaction (5):



This led to the re-precipitation of NiO within the original corrosion scale. The continuous metal dissolution/oxide re-precipitation processes resulted in the formation of voids and cracks in the oxide scales. In addition, Cl^- destroyed the NiO scale through these voids, which was evidenced by the sudden drops of anode potential (Fig. 3c) and the cross-

sectional morphology of corrosion scale (Fig. 7c). The porous and loose NiO scale was poorly adhered to nickel substrate, and thus the nickel substrate was seriously corroded by molten carbonate. When the oxide scales were spalled from the substrate due to the interstress within the scales and the mechanical action of oxygen bubbles, the bare nickel substrate was re-passivated and new oxide scale formed under anodic polarization. The passivation/spallation/re-passivation cycles continued until the nickel anode was completely depleted. Overall, Cl^- was not consumed during the electrolysis and acted as a corrosion catalyst to sustain the circulation of nickel dissolution and NiO re-precipitation processes, which significantly accelerated the corrosion of nickel anodes.

3.4. The protection effect of CaCO_3 on the corrosion of nickel anode

As discussed above, the lifetime of nickel anodes in Cl^- -containing molten carbonate is closely related to the solubility and stability of corrosion products, which are affected by the melt basicity [38–40]. In order to predict the corrosion tendencies of nickel in Cl^- -containing molten carbonate, potential-basicity diagram of nickel was constructed. As shown in Fig. 10, NiCl_2 tends to form in the electrolyte with lower basicity ($\lg a(\text{Li}_2\text{O}) < -10.19$). NiCl_2 is soluble and unstable in molten carbonate and it could spontaneously react with Li_2O to regenerate NiO , thereby resulting in the formation of loose and unprotective NiO corrosion scales. By contrast, more stable NiO scale tends to form and cover the nickel substrate in the electrolyte with higher basicity ($\lg a(\text{Li}_2\text{O}) > -10.19$), which could act as a protective barrier layer against the Cl^- attack. Therefore, it is rational to hypothesize that increasing the melt basicity can improve the corrosion resistance of nickel anodes to Cl^- .

It has been reported that CaCO_3 is an effective additive to increase the melt basicity of molten carbonate [41,42], thereby reducing the solubility of the NiO cathode for molten carbonate fuel cells (MCFC) applications. Accordingly, CaCO_3 was selected as the protective additive into Cl^- -containing molten carbonate to improve the corrosion resistance of nickel anodes. To evaluate the corrosion protection performance of CaCO_3 , galvanostatic polarization of nickel anodes was conducted in Cl^- -containing melts without or with CaCO_3 addition. The corresponding melt composition and gas atmosphere in each case are listed in Table 2, and the anode potential-time plots during the electrolysis are shown in Fig. 11. In CaCO_3 -free molten carbonate, nickel anodes underwent severe corrosion, and thus the anode potential could not reach a steady state (Fig. 11a). Besides, the observed regular potential oscillations were caused by the periodical forming and stripping of corrosion scales. After adding 5 wt% CaCO_3 into the electrolyte, the anode potential shifted positively to oxygen evolution potential (~ 0.5 V) within 900 s and remained stable during the subsequent electrolysis (Fig. 11b). Therefore, the addition of CaCO_3 effectively protected the nickel substrate from further dissolution and corrosion.

To further evaluate the protection performance of CaCO_3 on nickel anode under more acidic working atmosphere, galvanostatic electrolysis was carried out under 14 vol% CO_2 -Ar atmosphere. As shown in Fig. 11c and d, nickel anode could not work stably in CaCO_3 -free electrolyte, while in contrast with that nickel anode can be passivated in the electrolyte containing 5 wt% CaCO_3 . However, the anode potential oscillations were observed after it remained stable for ~ 4000 s, suggesting that the formed protective oxide scale was damaged by chloride. It was obvious that the corrosion protection performance of CaCO_3 on nickel anode was weakened under 14 vol% CO_2 -Ar atmosphere. Consequently, 10 wt% CaCO_3 was added to further increase the melt basicity of molten carbonate under more acidic working atmosphere. Comparing the anode potential-time plots shown in Fig. 11d and e, it was found that the

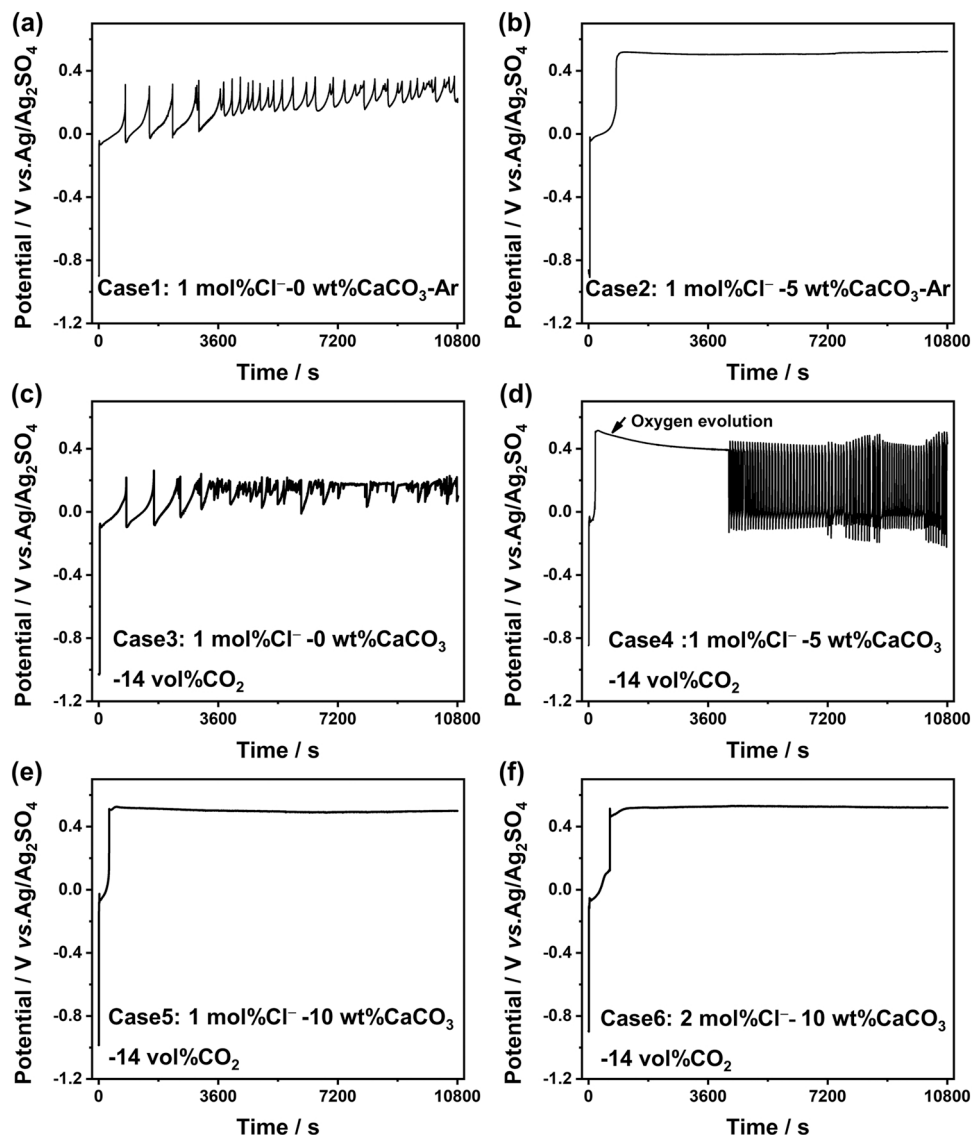


Fig. 11. Anode potential evolution over time during the galvanostatic electrolysis for 10,800 s at $I_{\text{anode}} = 200 \text{ mA/cm}^2$ in Cl^- -containing molten $\text{Li}_2\text{CO}_3\text{-Na}_2\text{CO}_3\text{-K}_2\text{CO}_3$ without or with CaCO_3 addition at 650 °C.

susceptibility of nickel anodes to chloride was reduced with increasing CaCO_3 addition. More importantly, nickel anode could even be passivated in the electrolyte containing 2 mol% Cl^- after adding 10 wt% CaCO_3 (Fig. 11f). This indicates that the increasing CaCO_3 addition increased the critical corrosion concentration of Cl^- .

Fig. 12a shows the optical images of nickel electrodes after the corrosion tests in Cl^- -containing electrolytes with different contents of CaCO_3 . In the case 1, 3 and 4, nickel anodes could not be passivated. The dark green and loose corrosion scales with poor adherence formed, which were easily removed by the washing treatments. By contrast, in the case 2, 5 and 6, nickel rods were all covered by the black and compact oxide scales, which were firmly attached to the substrate. The weight change results of nickel electrodes after the washing treatments are shown in Fig. 12b. In CaCO_3 -free electrolytes, the weight loss was mainly caused by the spallation of corrosion scales after the washing treatments. The weight loss of nickel anodes under argon and 14 vol% $\text{CO}_2\text{-Ar}$ atmospheres was -0.305 and -0.365 g cm^{-2} , respectively. When 5 wt% CaCO_3 was added, the weight of nickel electrode gained 0.042 g cm^{-2} under an argon atmosphere, and the weight loss under 14 vol% $\text{CO}_2\text{-Ar}$ was decreased to -0.296 g cm^{-2} . Thus, it can be

concluded that CaCO_3 can effectively protect the nickel anodes from Cl^- induced corrosion.

Overall, adding a certain amount of CaCO_3 can increase the melt basicity of molten carbonate, thereby improving the corrosion resistance of nickel anodes in the Cl^- -containing electrolytes.

4. Conclusions

The corrosion rate of nickel anodes was greatly affected by the chloride concentration in molten carbonate. There was a critical Cl^- concentration that induced the pitting corrosion of nickel anodes. A compact and protective NiO scale was prone to form and could act as a barrier layer against chloride below the critical Cl^- concentration of 0.2 mol%, and severe pitting corrosion happened when the Cl^- concentration was above 0.2 mol%. Under the guidance of potential-basicity diagram of nickel, CaCO_3 can increase the melt basicity of electrolyte and effectively protect the nickel anodes from corrosion. Overall, revealing the failure mechanism of nickel anodes in Cl^- -containing electrolytes and the protection effect of CaCO_3 is beneficial for the development of long-lasting inert anodes, which is crucial for molten

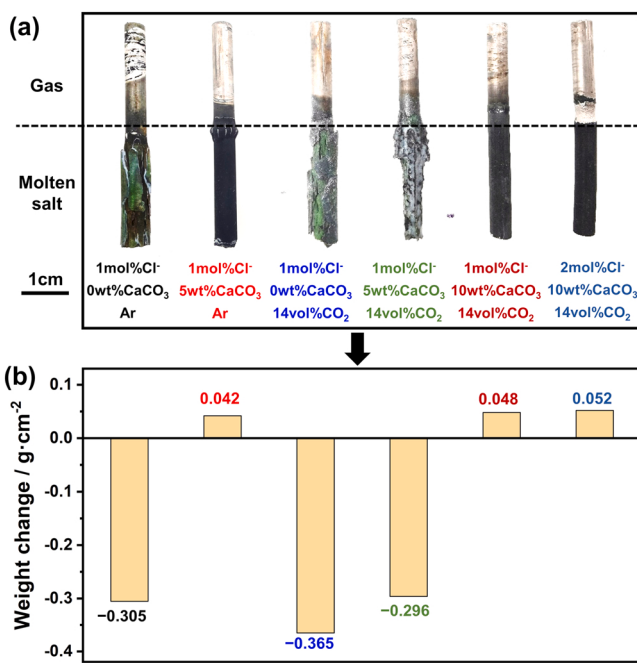


Fig. 12. Optical images (a) and weight changes (b) of nickel electrodes polarized for 10,800 s at $I_{\text{anode}} = 200 \text{ mA/cm}^2$ in Cl^- -containing molten $\text{Li}_2\text{CO}_3\text{-Na}_2\text{CO}_3\text{-K}_2\text{CO}_3$ without or with CaCO_3 addition at 650 °C.

carbonate electrolysis. Moreover, this work also contributes to the knowledge of the passivation process and pitting corrosion of metallic materials under anodic polarization in high-temperature molten salt media.

CRediT authorship contribution statement

Peilin Wang: Conceptualization, Methodology, Validation, Investigation, Writing – original draft, Writing – review & editing. **Kaifa Du:** Methodology, Investigation, Writing – review & editing. **Mengyi Tang:** Investigation, Writing – review & editing. **Huayi Yin:** Conceptualization, Methodology, Writing – review & editing. **Dihua Wang:** Conceptualization, Methodology, Writing – review & editing, Funding acquisition.

Declaration of Competing Interest

The authors declare that they have no known competing financial interests or personal relationships that could have appeared to influence the work reported in this paper.

Data Availability

The raw/processed data required to reproduce these findings cannot be shared at this time due to technical or time limitations.

Acknowledgement

This work was supported by the National Natural Science Foundation of China (No. 51874211 and 52031008).

References

- [1] R. Jiang, M. Gao, X. Mao, D. Wang, Advancements and potentials of molten salt CO_2 capture and electrochemical transformation (MSCC-ET) process, *Curr. Opin. Electrochem.* 17 (2019) 38–46.
- [2] Y. Chen, M. Wang, J. Zhang, J. Tu, J. Ge, S. Jiao, Green and sustainable molten salt electrochemistry for the conversion of secondary carbon pollutants to advanced carbon materials, *J. Mater. Chem. A* 9 (2021) 14119–14146.
- [3] L. Barelli, G. Bidini, G. Cinti, J. Milewski, High temperature electrolysis using molten carbonate electrolyzer, *Int. J. Hydrogen Energy* 46 (2021) 14922–14931.
- [4] H. Yin, X. Mao, D. Tang, W. Xiao, L. Xing, H. Zhu, D. Wang, D.R. Sadoway, Capture and electrochemical conversion of CO_2 to value-added carbon and oxygen by molten salt electrolysis, *Energy Environ. Sci.* 6 (2013) 1538–1545.
- [5] H. Yin, D. Tang, H. Zhu, Y. Zhang, D. Wang, Production of iron and oxygen in molten $\text{K}_2\text{CO}_3\text{-Na}_2\text{CO}_3$ by electrochemically splitting Fe_2O_3 using a cost affordable inert anode, *Electrochim. Commun.* 13 (2011) 1521–1524.
- [6] K. Zheng, X. Cheng, Y. Dou, H. Zhu, D. Wang, Electrolytic production of Nickel-cobalt magnetic alloys from solid oxides in molten carbonates, *J. Electrochem. Soc.* 164 (2017) E422–E427.
- [7] X. Cheng, D. Tang, D. Tang, H. Zhu, D. Wang, Cobalt powder production by electro-reduction of Co_3O_4 granules in molten carbonates using an inert anode, *J. Electrochem. Soc.* 162 (2015) E68–E72.
- [8] J. Huang, K. Du, P. Wang, H. Yin, D. Wang, Electrochemical preparation and homogenization of face-centered FeCoNiCu medium entropy alloy electrodes enabling oxygen evolution reactions, *Electrochim. Acta* 378 (2021).
- [9] J. Ren, A. Yu, P. Peng, M. Lefler, F.F. Li, S. Licht, Recent advances in Solar Thermal Electrochemical Process (STEP) for carbon neutral products and high value nanocarbons, *Acc. Chem. Res.* 52 (2019) 3177–3187.
- [10] H.V. Ijije, C. Sun, G.Z. Chen, Indirect electrochemical reduction of carbon dioxide to carbon nanopowders in molten alkali carbonates: process variables and product properties, *Carbon* 73 (2014) 163–174.
- [11] Z. Chen, Y. Gu, L. Hu, W. Xiao, X. Mao, H. Zhu, D. Wang, Synthesis of nanostructured graphite via molten salt reduction of CO_2 and SO_2 at a relatively low temperature, *J. Mater. Chem. A* 5 (2017) 20603–20607.
- [12] D.R. Sadoway, Inert anodes for the Hall-Heroult cell: the ultimate materials challenge, *JOM-J. Miner. Met. Mater. Soc.* 53 (2001) 34–35.
- [13] W. Wei, S. Geng, D. Xie, F. Wang, High temperature oxidation and corrosion behaviours of Ni-Fe-Cr alloys as inert anode for aluminum electrolysis, *Corros. Sci.* 157 (2019) 382–391.
- [14] V. Chapman, B.J. Welch, M. Skyllas-Kazacos, High temperature oxidation behaviour of Ni-Fe-Co anodes for aluminium electrolysis, *Corros. Sci.* 53 (2011) 2815–2825.
- [15] Y. Sakamura, M. Iizuka, Applicability of nickel ferrite anode to electrolytic reduction of metal oxides in $\text{LiCl-Li}_2\text{O}$ melt at 923 K, *Electrochim. Acta* 189 (2016) 74–82.
- [16] K. Du, R. Yu, M. Gao, Z. Chen, X. Mao, H. Zhu, D. Wang, Durability of platinum coating anode in molten carbonate electrolysis cell, *Corros. Sci.* 153 (2019) 12–18.
- [17] X. Cheng, L. Fan, H. Yin, L. Liu, K. Du, D. Wang, High-temperature oxidation behavior of Ni-11Fe-10Cu alloy: growth of a protective oxide scale, *Corros. Sci.* 112 (2016) 54–62.
- [18] X. Cheng, H. Yin, D. Wang, Rearrangement of oxide scale on Ni-11Fe-10Cu alloy under anodic polarization in molten $\text{Na}_2\text{CO}_3\text{-K}_2\text{CO}_3$, *Corros. Sci.* 141 (2018) 168–174.
- [19] D. Tang, K. Zheng, H. Yin, X. Mao, D.R. Sadoway, D. Wang, Electrochemical growth of a corrosion-resistant multi-layer scale to enable an oxygen-evolution inert anode in molten carbonate, *Electrochim. Acta* 279 (2018) 250–257.
- [20] K. Zheng, K. Du, X. Cheng, R. Jiang, B. Deng, H. Zhu, D. Wang, Nickel-Iron-Copper alloy as inert anode for ternary molten carbonate electrolysis at 650 °C, *J. Electrochem. Soc.* 165 (2018) E572–E577.
- [21] K. Du, K. Zheng, Z. Chen, H. Zhu, F. Gan, D. Wang, Unusual temperature effect on the stability of nickel anodes in molten carbonates, *Electrochim. Acta* 245 (2017) 410–416.
- [22] W. Chen, C. Lee, H. Ho, Purification of lithium carbonate from sulphate solutions through hydrogenation using the Dowex G26 resin, *Appl. Sci.* 8 (2018).
- [23] G. Kuang, Y. Liu, H. Li, S. Xing, F. Li, H. Guo, Extraction of lithium from β -spodumene using sodium sulfate solution, *Hydrometallurgy* 177 (2018) 49–56.
- [24] G. Steinhauser, Cleaner production in the Solvay Process: general strategies and recent developments, *J. Clean. Prod.* 16 (2008) 833–841.
- [25] P. Meshram, B.D. Pandey, T.R. Mankhand, Extraction of lithium from primary and secondary sources by pre-treatment, leaching and separation: a comprehensive review, *Hydrometallurgy* 150 (2014) 192–208.
- [26] Z. Chen, B. Deng, K. Du, X. Mao, H. Zhu, W. Xiao, D. Wang, Flue-gas-derived sulfur-doped carbon with enhanced capacitance, *Adv. Sustain. Syst.* 1 (2017).
- [27] P. Wang, K. Du, Y. Dou, H. Zhu, D. Wang, Corrosion behaviour and mechanism of nickel anode in SO_4^{2-} -containing molten $\text{Li}_2\text{CO}_3\text{-Na}_2\text{CO}_3\text{-K}_2\text{CO}_3$, *Corros. Sci.* 166 (2020).
- [28] J. Soltis, Passivity breakdown, pit initiation and propagation of pits in metallic materials – review, *Corros. Sci.* 90 (2015) 5–22.
- [29] D.A. Shores, B.P. Mohanty, Role of chlorides in hot corrosion of a cast Fe–Cr–Ni alloy. Part II: thermochemical model studies, *Corros. Sci.* 46 (2004) 2909–2924.
- [30] B. Zhang, J. Wang, B. Wu, X.W. Guo, Y.J. Wang, D. Chen, Y.C. Zhang, K. Du, E. E. Oguzie, X.L. Ma, Unmasking chloride attack on the passive film of metals, *Nat. Commun.* 9 (2018) 2559.
- [31] P. Marcus, V. Maurice, H.H. Strehblow, Localized corrosion (pitting): a model of passivity breakdown including the role of the oxide layer nanostructure, *Corros. Sci.* 50 (2008) 2698–2704.
- [32] S. Abu Kassim, J.A. Thor, A. Abu Seman, T.K. Abdullah, High temperature corrosion of Hastelloy C22 in molten alkali salts: the effect of pre-oxidation treatment, *Corros. Sci.* 173 (2020).
- [33] A. Ruh, M. Spiegel, Thermodynamic and kinetic consideration on the corrosion of Fe, Ni and Cr beneath a molten KCl-ZnCl_2 mixture, *Corros. Sci.* 48 (2006) 679–695.
- [34] M. Cassir, M. Olivry, V. Albin, B. Malinowska, J. Devynck, Thermodynamic and electrochemical behavior of nickel in molten $\text{Li}_2\text{CO}_3\text{-Na}_2\text{CO}_3$ modified by addition of calcium carbonate, *J. Electroanal. Chem.* 452 (1998) 127–137.

- [35] Z. Duan, C. Man, C. Dong, Z. Cui, D. Kong, L. wang, X. Wang, Pitting behavior of SLM 316L stainless steel exposed to chloride environments with different aggressiveness: pitting mechanism induced by gas pores, *Corros. Sci.* 167 (2020).
- [36] G. Sander, V. Cruz, N. Bhat, N. Birbilis, On the in-situ characterisation of metastable pitting using 316L stainless steel as a case study, *Corros. Sci.* 177 (2020).
- [37] Z. Liu, P. Guo, C. Zeng, Effect of Dy on the corrosion of NiO/Ni in molten $(0.62\text{Li}_2\text{O} \cdot 0.38\text{K}_2\text{CO}_3)$, *J. Power Sources* 166 (2007) 348–353.
- [38] H. Flood, T. Furland, The acidic and basic properties of oxides, *Acta Chem. Scand.* 1 (1947) 592–604.
- [39] A. Nishikata, H. Numata, T. Tsuru, Electrochemistry of molten salt corrosion, *Mater. Sci. Eng. A* 146 (1991) 15–31.
- [40] M.L. Orfield, D.A. Shores, The solubility of NiO in binary mixtures of molten carbonates, *J. Electrochem. Soc.* 136 (1989).
- [41] K. Tanimoto, Y. Miyazaki, M. Yanagida, S. Tanase, T. Kojima, N. Ohtori, H. Okuyama, T. Kodama, Cell performance of molten-carbonate fuel cell with alkali and alkaline-earth carbonate mixtures, *J. Power Sources* 39 (1992) 285–297.
- [42] B. Malinowska, M. Cassir, F. Delcorso, J. Devynck, Behaviour of nickel species in molten $\text{Li}_2\text{CO}_3 + \text{Na}_2\text{CO}_3 + \text{K}_2\text{CO}_3$ Part 1. Thermodynamic approach and electrochemical characterization under $P(\text{CO}_2) = 1 \text{ atm}$, *J. Electroanal. Chem.* 389 (1995) 21–29.